Aeroelastic Simulation of High-Aspect Ratio Wings with Intermittent Leading-Edge Separation*

Yinan Wang†, Xiaowei Zhao‡
University of Warwick, Coventry CV4 7AL, United Kingdom
Rafael Palacios§
Imperial College, London SW7 2AZ, United Kingdom,
Keisuke Otsuka¶
Department of Aerospace Engineering, Tohoku University, Sendai 980-8579, Japan

We present a medium-fidelity aeroelastic framework for computing intermittently separating 3D flows around high-aspect ratio wings with a significantly reduced computational cost than CFD-based method. To achieve that, we propose a modified 3D vortex panel method with leading-edge separation controlled by leading-edge suction parameter theory, and its incorporation in a coupled aeroelastic solver for the dynamic response of these systems. Numerical verifications and simulations are presented on both attached and separated aeroelastic test cases, demonstrating the method on post-flutter limit-cycle oscillation of a cantilever wing, and leading-edge separation on a deploying wing a complex kinematic response. In both cases we were able to capture 3D interactions on intermittently separating dynamic flow fields using a low computational cost.

Nomenclature

Symbols

$\mathcal{A}$	panel influence coefficient matrix
$\mathbf{A}$	structural A-matrix
A	Eldredge function parameter
A_0	leading-edge suction parameter
$A_{0,crit}$	critical leading-edge suction parameter
a	distance between e.a. and a.c.
$\mathbf{B}$	structural B-matrix

*Part of the work was presented as a technical article at SciTech 2021, January 2021 virtual conference, AIAA 2021-1708.
†Department of Engineering, AIAA Member (contact author:yinan.wang@warwick.ac.uk)
‡Department of Engineering
§Department of Aeronautics, AIAA Member
¶Department of Aerospace Engineering, AIAA Associate Fellow

$\mathbf{b}$	panel binormal vector
$C(k)$	Theodorsen's lift deficiency function
c	chord
$\mathbf{E}$	structural E-matrix
$\mathbf{f}_A$	structural external forces
$\mathbf{G}$	structural G-matrix
$\mathbf{G}_A, \mathbf{G}_C, \mathbf{G}_S$	operators in coupled aeroelastic system
h	heave
K	Eldredge function parameter
$\mathbf{k}$	panel tangential vector
k	reduced frequency
$\mathbf{M}, \mathbf{P}$	coefficient matrix
$\mathbf{n}$	normal vector
p	pressure
$\mathbf{r}$	inertial position of structural nodes
$\mathbf{T}$	inertial orientation of structural nodes
t	time
U_∞	freestream flow speed
$\mathbf{u}, \mathbf{v}$	velocity vector
$\mathbf{v}_\infty$	freestream velocity
α	angle of attack
β	displacement body thickness
Γ	circulation
γ	vorticity
δ	panel size parameter
θ	chordwise location on aerofoil using $1 - \cos$ mapping
λ	distance between c.m. and e.a.

ρ	density
ξ	global coordinate
Φ	velocity potential
$\boldsymbol{\omega}$	angular velocity
ω	angular frequency
Subscripts	
i, j	index
L	on the lower surface
m, n, p	panel indices
U	on the upper surface
u	panel u-direction
v	panel v-direction
w	wake
∞	freestream
$+$	panel in the positive tangential direction
$-$	panel in the negative tangential direction
Superscripts	
LE	at leading-edge
TE	at trailing-edge
Symbols	
$\dot{\bullet}$	temporal derivative
$\tilde{\bullet}$	cross-product operator
$\|\|\bullet\|\|$	norm
bold	a vector of quantities (in a matrix-vector equation)

I. Introduction

The simulation of unsteady aeroelastic response is very important in the design and control of very flexible, morphing, or deployable wings and other lifting surfaces. Despite the continuous growth of processing power, the computational

requirement for CFD simulations of unsteady aerodynamic response for full-size aero-structures is still high by today's standards, especially for high-Reynolds flows with significant separation. As a result, potential flow methods, such as the unsteady vortex-lattice method and vortex panel method, remain a powerful category of low-order methods in analysing the low-speed dynamic aeroelasticity of slender lifting surfaces, including HALE aircraft[1, 2], horizontal-axis wind turbines[3, 4] and helicopter rotor blades[5].

Pure potential flow models lack the ability to account for the nonlinearity in the lift curve for attached flows, and stall for separated flows. Both are the result of boundary layer physics and are key to simulating limit-cycle oscillations and other unsteady aeroelastic responses. However, simulating these phenomena requires flow information that is not directly available from inviscid solutions.

A common approach to address this issue is to partially replace aerofoil data in potential flow solutions with steady or unsteady reduced-order models built using data from either high-fidelity CFD simulations or experimental measurements. Meanwhile the three-dimensional interactions between them is still retained using lifting-line type corrections [6–8]. Leishmann-Beddoes[9, 10] or ONERA[11, 12] are two most widely used dynamic stall models found in these applications. However these approaches lose the predictive capability that made panel methods attractive.

Within the framework of potential flow models, approaches to combine boundary layer theory with 2D or 3D inviscid formulation had great success before advances in computational power permitted the widespread adoption of CFD simulation. XFoil[13, 14] is perhaps the most well-known example in this area. These formulations typically use transpiration velocity[15] or displacement thickness[14] theories to couple classical one-dimensional boundary layer theory with a potential flow model. On the other hand, it is well-established that dynamic loads from fully separated flows can be modelled with vortex shedding[16] in an inviscid solution. For streamlined bodies, this is complicated by the need to predict the onset of separation, which, again, requires tuning by high-order simulations or experimental data, or for the boundary layer to be modelled in detail. It is worth noting that incorporating even the most basic boundary layer equations necessitates elaborate numerical schemes featuring strong coupling between the inviscid solution and the boundary layer equations, in order to avoid numerical instability near stagnation points including trailing edge or any separation point[15].

Efforts to incorporate separation criterion using the boundary layer theory in 3D unsteady vortex-lattice method (UVLM) or panel methods have been made previously[17]. A recent work by Ramos-Garcia[3] has presented a coupled aeroelasticity framework for horizontal-axis wind turbines. It uses a fully coupled 2D boundary-layer / unsteady panel solver with additional correction for the effect of radial flow on the boundary layer in cylindrical coordinates. The model is able to predict the onset of quasi-static separation bubbles, with the separation point predicted by parameters in the boundary layer, and has obtained very good agreement with experimental data. Meanwhile, Prasad *et al*[18] have proposed a similar method that models separation with dynamic vortex shedding in a panel solver.

Ramesh *et al*[19] has proposed the critical leading-edge suction parameter (LESP) to predict the occurrence of

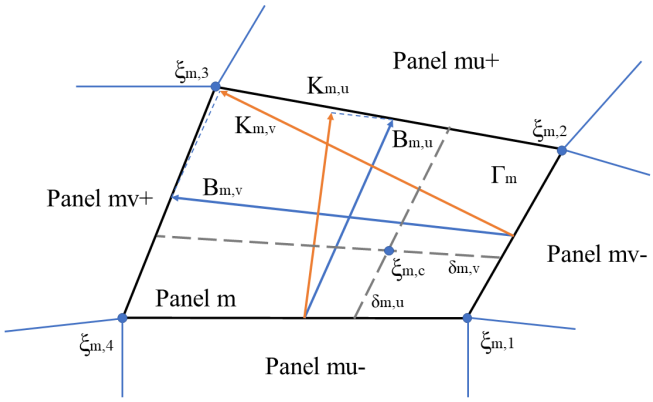

Fig. 1 Definition of a vortex panel used in this work. The normal vector points outwards from the page.

dynamic separation and the strength of the separated vortex at the leading edge (LE). The parameter is based on the behaviour of the boundary layer near the leading edge, but can be used without the need to apply a full boundary-layer model. It is tuned using high-order simulations and is particular to an aerofoil at a given Reynolds number. It has been demonstrated that the LESP theory is able to capture the lift, drag and moment responses in 2D dynamic stall cases for a thin aerofoil to a high accuracy, when used together with a discrete-vortex method .

In this work, we present a coupled aeroelastic solver for intermittently separating flows. By using a 3D vortex panel formulation, we extend the LESP theory to three dimensions and incorporate the formulation in an unsteady aeroelasticity solver. Attention is paid to the treatment of reattachment in the extension to 3D. Numerical cases will then be used to demonstrate this method, including a folding wing deployment, as well as stall flutter and limit-cycle oscillation on slender wing.

II. Aerodynamic Formulation

In this section, we discuss the inviscid aerodynamic formulation (more precisely, the unsteady vortex panel method) used in this work, as well as separated flow modelling using the LESP parameter. Most part of the formulation follows the standard panel method and is included here for completeness. Only minor modifications are made to the numerical scheme in order to achieve better convergence at relatively low discretisations.

A. Lattice Discretisation

Consider a lifting surface in a freestream flow $\mathbf{u}_\infty(t)$ and subject to external turbulent velocity field $\mathbf{v}_{turb}(\boldsymbol{\xi}, t)$. In the unsteady vortex-lattice method, the bound vortex sheet around a lifting surface is discretised into a mesh consisting of M quadrilateral vortex rings, or constant strength doublet panels, of strength $\Gamma_m(t)$, where $m \in [1, M]$. The corners of the m-th panel are located at coordinates $\boldsymbol{\xi}_{m,1}(t)$, $\boldsymbol{\xi}_{m,2}(t)$, $\boldsymbol{\xi}_{m,3}(t)$, and $\boldsymbol{\xi}_{m,4}(t)$ respectively. The corner nodes move

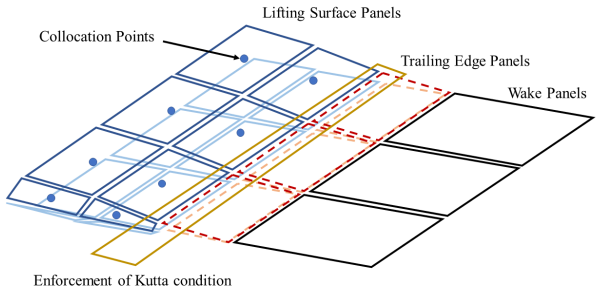

Fig. 2 Illustration of discretised vortex panels, wingtips, and the trailing edge

in the inertial frame with velocities $\dot{\boldsymbol{\xi}}_{m,1}$ to $\dot{\boldsymbol{\xi}}_{m,4}$, here noted as $\mathbf{v}^n_{m,1}$ to $\mathbf{v}^n_{m,4}$.

A collocation point, at which boundary conditions are enforced, is defined on each bound panel, with an associated unit normal vector for the panel $\mathbf{n}_m$. The in-plane tangential vectors are defined as $\mathbf{k}_{m,u}$ and $\mathbf{k}_{m,v}$, perpendicular to vectors connecting the midpoints between opposing edges, $\mathbf{b}_{m,u}$ and $\mathbf{b}_{m,v}$. The panel size in the two tangential directions are defined as $(||\mathbf{k}_{m,u}||, ||\mathbf{k}_{m,v}||)$. Figure 1 is an illustration of the panel definition presented here.

In addition, there are also $2N$ newly shed trailing-edge panels where N is the number of segments in which the trailing edge is divided into, and $P(t)$ wake panels in the wake vortex sheet. These have vorticities of $\Gamma^{TE}_n(t)$ and $\Gamma^w_p(t)$ respectively, where $n \in [1, 2N]$ and $p \in [1, P]$. The trailing-edge (TE) panels and wake panels are defined in the same way as the lifting surface panels, only that they lack an associated collocation point and that the nodes of the wake panels are not rigidly bound to the structure and move with the local flow velocity.

The placement of the collocation point is dependent on the sizes of the adjacent panels in order to achieve faster convergence with non-uniform panel sizes. The location of the collocation point $\boldsymbol{\xi}_{m,c}$ on the m-th panel is expressed as a linear combination of its corners as

$$\boldsymbol{\xi}_{m,c} = \begin{pmatrix} \delta_{m,u} & 1-\delta_{m,u} \end{pmatrix} \begin{pmatrix} \boldsymbol{\xi}_{m,1} & \boldsymbol{\xi}_{m,2} \\ \boldsymbol{\xi}_{m,4} & \boldsymbol{\xi}_{m,3} \end{pmatrix} \begin{pmatrix} \delta_{m,v} \\ 1-\delta_{m,v} \end{pmatrix}, \tag{1}$$

where $\delta_{m,u}$ and $\delta_{m,v}$ are size parameters in the in-plane u and v directions, written as

$$\delta_{m,u} = \frac{||\mathbf{k}_{m,u}|| + ||\mathbf{k}_{m,u-}||}{||\mathbf{k}_{m,u+}|| + 2||\mathbf{k}_{m,u}|| + ||\mathbf{k}_{m,u-}||}, \tag{2}$$

$$\delta_{m,v} = \frac{||\mathbf{k}_{m,v}|| + ||\mathbf{k}_{m,v-}||}{||\mathbf{k}_{m,v+}|| + 2||\mathbf{k}_{m,v}|| + ||\mathbf{k}_{m,v-}||}. \tag{3}$$

Here the subscripts + and − indicate adjacent panels in the positive and negative tangential directions respectively.

The instantaneous flow field is given as the superposition of the freestream flow, incoming turbulence, and the

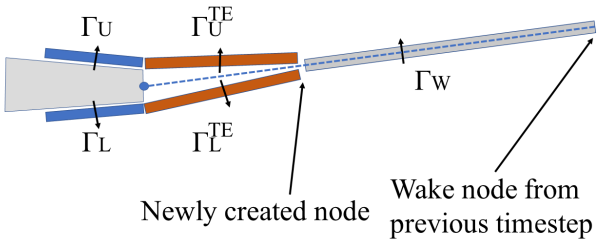

Fig. 3 Illustration of the shedding from trailing edge.

induced velocity fields from singularity elements (including lifting surface, trailing edge, and wake panels) and the wake. The induced velocity field generated by the m-th vortex ring (with corners located at $\boldsymbol{\xi}_{m,1}(t)$, $\boldsymbol{\xi}_{m,2}(t)$, $\boldsymbol{\xi}_{m,3}(t)$, and $\boldsymbol{\xi}_{m,4}(t)$) at position $\boldsymbol{\xi}$ is specified by the aerodynamic influence coefficient based on Biot–Savart law[20] and takes the form of $\mathcal{A}_m(\boldsymbol{\xi})\Gamma_m$. The velocity field is thus written as

$$\mathbf{v}_{ind}(\boldsymbol{\xi},t) = \sum_m \mathcal{A}_m(\boldsymbol{\xi},t)\Gamma_m(t) + \sum_n \mathcal{A}_n^{TE}(\boldsymbol{\xi},t)\Gamma_n^{TE}(t) + \sum_p \mathcal{A}_p^{w}(\boldsymbol{\xi},t)\Gamma_p^{w}(t) + \mathbf{u}_\infty(t) + \mathbf{v}_{turb}(\boldsymbol{\xi},t). \tag{4}$$

B. Boundary Conditions and Time Marching

A number of boundary conditions compatible with potential flow methods have been detailed in the literature[3, 14, 20]. For this work, the zero normal flow condition will be enforced at every collocation point. Thus at each collocation point,

$$(\mathbf{v}_m - \mathbf{v}_m^c) \cdot \mathbf{n}_m = 0, \tag{5}$$

where $\mathbf{v}_m^c$ is the inertial velocity at the m-th collocation point, given by the weighted mean of the inertial velocity of the associated panel corner points $\mathbf{v}_m^n$.

We consider aerofoils with a finite but small trailing-edge thickness. As shown in figure 3, no vortex panels or collocation points are placed across the trailing edge, rather the trailing edge gap is bridged by two trailing vortex panels forming the newly shed vortex sheet. The Kutta condition[20] requires all vorticity to be shed at the TE, thus the total vorticity along the trailing edge is zero everywhere and for every pair of trailing edge panels, eq. (6), is enforced. In addition, another equation, eq. (7) is enforced to remove the ambiguity associated with the strengths of upper and lower

trailing edge panel. Therefore for each pair of trailing edge panels, the trailing edge boundary conditions are written as

$$(\Gamma_U - \Gamma_U^{TE}) - (\Gamma_L - \Gamma_L^{TE}) = 0, \tag{6}$$

$$\Gamma_U^{TE} + \Gamma_L^{TE} = 0. \tag{7}$$

In this work, we use the method suggested by Ramesh[19] to place the newly created panel nodes that was shed from the trailing edge. At each timestep, the node for the newly created vortex panel is placed at one-third of the distance from the shedding edge to the end of the most recently shed wake panel. Note that for a flat plate at low angles of attack, this is equivalent to placing the new panel edge at a distance of $|\mathbf{u}_\infty|dt/2$ from the trailing edge in a central-difference implicit scheme. If no vortex was shed at the previous timestep, then this panel is placed at $|\mathbf{u}_\infty|dt/2$ in the tangential direction from the trailing edge. This scheme is numerically stable and removes the explicit dependence on the global quantity $\mathbf{u}_\infty$.

At each timestep, the flow field is obtained by solving the matrix-vector equation for the unknown surface panel strengths $\mathbf{\Gamma}$ and trailing edge panel strengths $\mathbf{\Gamma}^{TE}$ using influence coefficients, non-peneration and trailing edge boundary conditions. The matrix-vector equation assumes the form of

$$\begin{pmatrix} \mathbf{M}_{inf} \\ \mathbf{M}_{kutta} \end{pmatrix} \begin{pmatrix} \mathbf{\Gamma} \\ \mathbf{\Gamma}^{TE} \end{pmatrix} = \begin{pmatrix} \mathbf{v}_{rhs} \\ \mathbf{0} \end{pmatrix}, \tag{8}$$

of which $\mathbf{M}_{inf} \in \mathbb{R}^{M\times(M+2N)}$ contains the non-penetration conditions (5) and $\mathbf{M}_{kutta} \in \mathbb{R}^{2N\times(M+2N)}$ enforces the Kutta conditions (eqs. (6) and (7)).

Upon resolving the flow field at each timestep, the wake panels corner nodes are advected with a first-order explicit scheme,

$$\boldsymbol{\xi}(t_{i+1}) = \boldsymbol{\xi}(t_i) + \mathbf{v}_{ind}dt, \tag{9}$$

by computing $\mathbf{v}_{ind}$ at each corner node's locations using equation (4). During the advection process, each pair of upper and lower trailing edge panels are also merged into one new wake panel with strength $\Gamma_U^{TE} - \Gamma_L^{TE}$. The sign is due to the definition of the panel normal direction.

Finally, due to the non-penetration boundary condition, any singularity that strictly follows its local induced velocity will remain outside of any solid body in a Lagrangian formulation. However, in a vortex ring panel formulation, the condition is only enforced at collocation points themselves. A number of treatments have been proposed to treat vortex particles (or in the case of UVLM, panel corner points) that cross into solid bodies[21]. In this work, a displacement body around solid bodies is defined by displacing the body mesh by $\beta|\mathbf{B}|\hat{n}$ where $\hat{n}$ is the local normal direction, $\mathbf{B}$ is

the local panel size and β is a thickness parameter specifying the size of the displacement body. Any panel corner that crosses the displacement body during advection will be reflected at the point of crossing.

C. Computation of Aerodynamic Load

The local pressure $p(\boldsymbol{\xi}, t)$ at a position $\boldsymbol{\xi}$ on the aerodynamic surface is given by the unsteady Bernoulli's equation as a function of the local relative velocity $\mathbf{v}_m^r$ and the potential function Φ as

$$p(\boldsymbol{\xi}, t) - p_\infty = -\rho \left(\frac{\mathbf{v}^r(\boldsymbol{\xi}, t)^2}{2} + \frac{d\Phi(\boldsymbol{\xi}, t)}{dt} \right). \tag{10}$$

The constant-strength doublet panel used in this work is a low-order element. As a result, the flow field may be inaccurate when evaluated at a point within one panel width from the aerodynamic surface. To address this in this work, the flow velocity is computed at collocation points as[20]

$$\mathbf{v}_{ext,m} = \frac{1}{2} \left(\frac{\Gamma_{m,u+} - \Gamma_{m,u-}}{||\mathbf{k}_{m,u}||} \frac{\mathbf{b}_{m,v}}{||\mathbf{b}_{m,v}||} + \frac{\Gamma_{m,v+} - \Gamma_{m,v-}}{||\mathbf{k}_{m,v}||} \frac{\mathbf{b}_{m,u}}{||\mathbf{b}_{m,u}||} \right) + \mathbf{v}_{ind,m}, \tag{11}$$

and the relative velocity to the local aerodynamic surface is given by $\mathbf{v}_m^r = \mathbf{v}_{ext,m} - \mathbf{v}_m^c$.

The surface potential Φ is cast as a pseudoinverse problem where the potential at adjacent collocation points are related by their local surface velocities $\mathbf{v}^{ext}$ by

$$\Phi_{m,u+} - \Phi_{m,u} = (\mathbf{v}_{ext,m,u+} + \mathbf{v}_{ext,m})/2 \cdot (\boldsymbol{\xi}_{m,u+,c} - \boldsymbol{\xi}_{m,c}). \tag{12}$$

Accounting for the connectivities between panels, the above relation results in a set of equations relating the vector array with the velocity potential at every collocation point $\boldsymbol{\Phi}$ to the flow field $\mathbf{v}_{ext}$ as

$$\mathbf{P}_1 \boldsymbol{\Phi} = \mathbf{P}_2 \mathbf{v}_{ext}. \tag{13}$$

This equation is solved at every timstep by taking the pseudoinverse of $\mathbf{P}_1$. The time derivative of $\boldsymbol{\Phi}$ is then computed as a first-order finite difference.

D. Separation and the Critical Leading-Edge Suction Parameter

In this section, we shall discuss the augmentation of the standard vortex panel method with leading-edge separation, whose separation criterion is modelled using the critical leading-edge suction parameter first introduced by Ramesh[19]. First, a brief description of the original 2D theory will be provided, which will be followed by its extension to 3D lifting surfaces.

1. The LESP Model in 2D

In thin-aerofoil theory, if the flow around an aerofoil is regarded as being caused by a vorticity distribution $\gamma(\theta)$ along its chordline, then the distribution can be written in an expansion as

$$\gamma(\theta) = 2U_\infty \left[A_0 \frac{1+\cos\theta}{\sin\theta} + \sum_{i=1}^{i_{max}} A_i \sin(i\theta) \right], \tag{14}$$

where θ is related to the distance along chord from the leading edge x by $x = c(1-\cos\theta)/2$.

Ramesh[19] defined the leading-edge suction parameter of the aerofoil at a particular instant in time as the value of A_0. The LESP model states that leading-edge separation will take place whenever A_0 exceeds a critical value, the 'critical LESP', or $A_{0,crit}$. The separation will shed an amount of vorticity from the leading edge such that the instantaneous A_0 is reduced to the value of $A_{0,crit}$. The value of $A_{0,crit}$ itself is a function of the aerofoil shape and Reynolds number, but which is independent of the kinematics at which the aerofoil is moving. As flow separation can occur in both positive and negative angles of attack, there exist $A_{0+,crit}$ and $A_{0-,crit}$ for the two directions, which will be of the same magnitude if the aerofoil is symmetric.

The original work by Ramesh[19] describes how the value of $A_{0,crit}$ can be identified for a given flow condition by resolving the flow field, more precisely, the skin friction coefficient, at the leading edge of heaving and pitching aerofoils in detail using high fidelity CFD simulations. One may also match the value of $A_{0,crit}$ so that the dynamic separation response matches known experimental data for given flow conditions and kinematics.

It was also pointed out that, for an aerofoil with finite leading-edge radius of curvature, the value A_0 is proportional to the tangential velocity at the leading edge. The critical LESP can thus be defined using this tangential velocity instead. The Fourier expansion was used in the original work as it can be computed from an integration of induced normal velocities on a thin aerofoil. For the current work, the leading-edge tangential velocity, v_{tanLE} is computed explicitly and will be used in the LESP theory instead. That is, we compare v_{tanLE} against given values of $v_{tanLE+,crit}$ and $v_{tanLE-,crit}$. Note that under the LESP theory, the Kutta condition can not be enforced at the leading edge as the shedding process is simplified. In reality the flow around a leading edge with finite curvature does not separate precisely from the leading edge but the LESP still serves to predict the correct amount of vorticity shed into the flow.

2. 3D Implementation of the LESP Model

In the extension of the theory to three dimensions, we make the assumption here that separation at the leading edge depends only on the local behaviour of the boundary layer there, and that the separation condition will remain equally valid in 3D if one considers a 2D section of the lifting surface around the leading edge. In the current 3D implementation, leading-edge separation is modelled as an additional vortex sheet shed from the leading edge. Rather than enforcing the Kutta condition, the strength of the shed vortex sheet at the leading edge is determined instead by

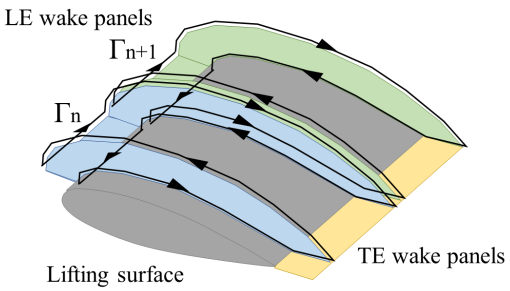

Fig. 4 Implementation of the separated vortex sheet, as well as its vortex ring representation, marking individual spanwise sections. This figure shows the treatment of the spanwise component, and how it relates to spanwise TE vortex lines.

the critical LESP criterion. Thus, the strength of the shedding at every spanwise location is given by Γ_t at time t that minimises the value of $||\Gamma_t - \Gamma_{t-1}||$ while satisfying $v_{tanLE-,crit} < v_{tanLE} < v_{tanLE+,crit}$.

A significant point in the application of separation to 3D is treating the chordwise boundary of the separation region. Here, we have modelled the separated vortex sheet as a horseshoe-shaped vortex sheet that always extends from the trailing edge (illustrated in Figure 4). Thus it is assumed that the separation region always initiates from the trailing edge and extends towards the leading edge. This assumption automatically satisfies the continuity of vorticity condition. Furthermore, this scheme also fulfils the requirement that when the separation stops, the model eventually reverts back to an attached-flow model, and does so without an added re-attachment formulation. It is easy to see that continuity condition dictates that the strength of the newly shed chordwise vortex sheet between the n-th and $n+1$-th section should be given as $\Gamma_n - \Gamma_{n+1}$, where Γ_n and Γ_{n+1} are the strengths of the newly shed LE vortex sheet of the two sections respectively.

One should note here that the strength of the separation in the chordwise direction is based on the continuity of vorticity argument. Near the wingtip, significant spanwise flow could significantly modify the behaviour of the boundary layer and affect the applicability of the 2D LESP model itself. However, such modification to the LESP theory is outside of the scope of this work.

3. Numerical Acceleration

Inviscid method based on singularity solutions form N-body problems and are of complexity $O(N^2)$. Both the fast multipole method (FMM) and the particle-particle, particle-mesh method (PPPM or P3M) are established ways to reduce the complexity of the N-body problem to $O(N \log N)$. In this work we utilise the STFMM fast multipole library[22] to accelerate the computation of wake-panel influence coefficients in every timestep.

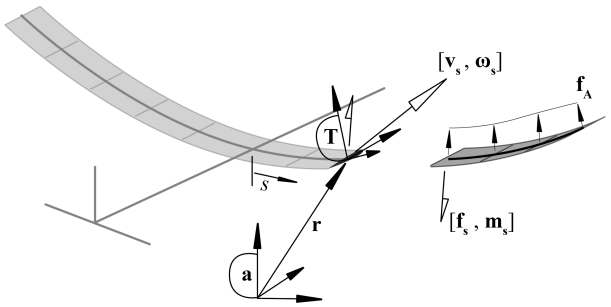

Fig. 5 Illustration of the variables in the structural model. The inertial frame is shown as the 'a'-frame.

III. Aeroelastic Integration

To complete the aeroelastic solver, we couple the aerodynamic solver to a structural model. A geometrically-exact beam model is used as it is a natural choice for the class of problems where the proposed aerodynamic model is applicable.

A. Structural Model

The structural model uses the intrinsic formulation for geometrically nonlinear beam dynamics developed in a previous work[23], where the method and numerical implementation is detailed. A summary of the formulation will be provided here for completeness.

The structure is defined as a collection of beams with linear elastic properties. At position s along the beam reference line, the structural properties are defined using beam-equivalent sectional mass and compliance matrices $\mathbf{M}_s(s)$ and $\mathbf{C}_s(s)$. The intrinsic states are sectional force and moment vectors $\mathbf{f}_s(s,t)$ and $\mathbf{m}_s(s,t)$ together with local velocity and angular velocity vectors $\mathbf{v}_s(s,t)$ and $\boldsymbol{\omega}_s(s,t)$, expressed in the local frame of reference. The structure is subject to distributed external force $\mathbf{f}_A(s,t)$.

The closed-form intrinsic beam formulation takes the form of

$$\mathbf{A}(s)\dot{\mathbf{x}} = \mathbf{B}(s)\mathbf{x} + \mathbf{G}(s,\mathbf{x})\mathbf{x} + \mathbf{E}(s)\mathbf{f}_A, \tag{15}$$

where the intrinsic state vector at location s is $\mathbf{x} = [\ \mathbf{v}_s^\top \quad \boldsymbol{\omega}_s^\top \quad \mathbf{f}_s^\top \quad \mathbf{m}_s^\top\ ]^\top$, and the matrices $\mathbf{A}$,$\mathbf{B}$,$\mathbf{E}$, and linear function $\mathbf{G}$ are functions of the local beam properties $\mathbf{M}$, $\mathbf{C}$ as well as connectivities. The nodal position $\mathbf{r}(s,t)$, and orientation relative to inertial frame as rotation matrix $\mathbf{T}(s,t)$, are expressed as an integration of the intrinsic states as

$$\dot{\mathbf{r}} = \mathbf{T}\mathbf{v}_s \tag{16a}$$

$$\dot{\mathbf{T}} = \mathbf{T}\tilde{\boldsymbol{\omega}}_s \tag{16b}$$

A modification from previous works on this formulation is the use of a backwards-Euler implicit time-marching scheme in the integration of equations (15) and (16) in time, providing a stable numerical scheme for any timestep size.

B. Aeroelastic Coupling

In the aeroelastic coupling scheme, weak coupling is used in the current framework, thus the aerodynamic and structural simulations are advanced alternately. We define a rigid-body connection on each aerodynamic node, connecting to a corresponding structural node. At each timestep, the nodal $\boldsymbol{\xi}$ and $\mathbf{v}^n$ on the aerodynamic panel mesh is evaluated from the structural degrees of freedom $\mathbf{v}_s$, $\boldsymbol{\omega}_s$, $\mathbf{r}$ and $\mathbf{T}$ at the associated structural reference node by the rigid-body kinematic transformation. This takes the form of

$$(\boldsymbol{\xi}|_t, \mathbf{v}^n|_t) = \mathbf{G}_C(\mathbf{v}_s|_t, \boldsymbol{\omega}_s|_t, \mathbf{r}|_t, \mathbf{T}|_t), \tag{17}$$

where $\mathbf{G}_C$ is a kinematic transformation. The aerodynamic model described in II.A is first advanced as

$$\mathbf{f}_A|_{t+1} = \mathbf{G}_A(\boldsymbol{\xi}|_t, \boldsymbol{\xi}|_{t-1}, \mathbf{v}^n|_t), \tag{18}$$

where $\mathbf{G}_A$ an the aerodynamic operator. The surface potential history at the previous timestep,$\boldsymbol{\xi}|_{t-1}$, is required to compute the derivative of $\boldsymbol{\xi}$ with time. Here the aerodynamic loads on the collocation points from the pressure computation are distributed to the panel corner nodes, and transferred back to the structure as an externally applied forces and moments $\mathbf{f}_A$. Finally the structural model from III.A is advanced as

$$(\mathbf{v}_s|_{t+1}, \boldsymbol{\omega}_s|_{t+1}, \boldsymbol{\gamma}_s|_{t+1}, \boldsymbol{\kappa}_s|_{t+1}, \mathbf{r}|_{t+1}, \mathbf{T}|_{t+1}) = \mathbf{G}_S(\mathbf{v}_s|_t, \boldsymbol{\omega}_s|_t, \boldsymbol{\gamma}_s|_t, \boldsymbol{\kappa}_s|_t, \mathbf{r}|_t, \mathbf{T}|_t, \mathbf{f}_A|_{t+1}), \tag{19}$$

where $\mathbf{G}_S$ is a structural operator. The use of weak coupling greatly simplifies the numerical scheme and avoids computing the Hessian for the aerodynamic model. This is justified as long as the timestep used is significantly smaller than the frequency of vortex shedding and any structural response that such shedding excites.

IV. Numerical Results and Verification

In this section, we present numerical verifications of the attached and separated aerodynamic models and aeroelastic coupling, followed by a simulation demonstrating the fully coupled aeroelastic solver using a folding wing deployment example. All results presented here are computed on a 16-core workstation.

A. Leading-Edge Separation on 2D Aerofoils with Prescribed Motion

In the first part, we demonstrate the use of LESP with the use of a 2D discrete-vortex simulation. In order to correspond with the 3D formulation presented in the previous sections, the aerofoil is discretised using point vortices,

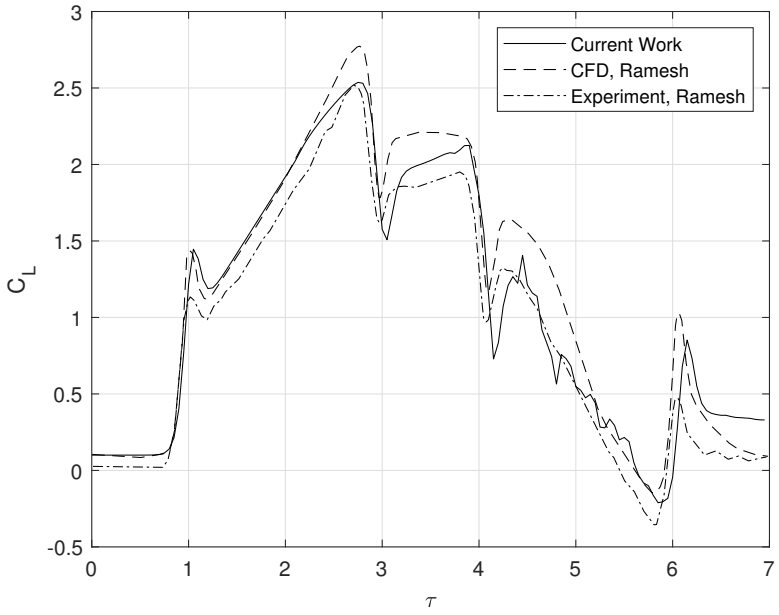

Fig. 6 Lift coefficient of an SD7003 aerofoil at $Re = 30000$ undergoing pitching motion about the leading edge.

which is the 2D equivalent to a vortex ring discretisation in 3D.

1. Pitching SD7003 aerofoil

As a first example, we demonstrate a model verification using a pitching SD7003 aerofoil. This case considers the aerofoil pitching about the leading edge, with the pitch angle α following the Eldredge function[24], $\alpha(t) = \alpha_{max} G(t)/\max(G(t))$. The Eldredge function $G(t)$ is written as

$$G(t) = \ln\left(\frac{\cosh(aU_\infty(t-t_1)/c)\cosh(aU_\infty(t-t_4)/c)}{\cosh(aU_\infty(t-t_2)/c)\cosh(aU_\infty(t-t_3)/c)}\right), \tag{20}$$

in which for a disturbance starting at t_1, the other variables are written as $t_2 = A/2K + t_1$, $t_3 = \pi A/4K + t_1$, and $t_4 = \pi A/4K + A/2K + t_1$. In this work we have selected the parameters $A = 11$, $\alpha_{max} = 25°$, and $K = 0.11$. Ramesh[19] identified the value of LESPc (A_0) under the conditions given to be 0.18 using CFD simulations. This case has been studied extensively by Ramesh and was used as an experimental validation for the LESP theory.

The aerofoil surface is discretised into 121 point vortices following the $1 - \cos$ distribution. Figure 6 shows the resultant lift experienced on the aerofoil. In this test case, leading-edge separation takes place after $\tau = 2$. It can be seen that the LESP implementation is able to capture the dynamic lift response when compared to experimental measurements and CFD simulations[19].

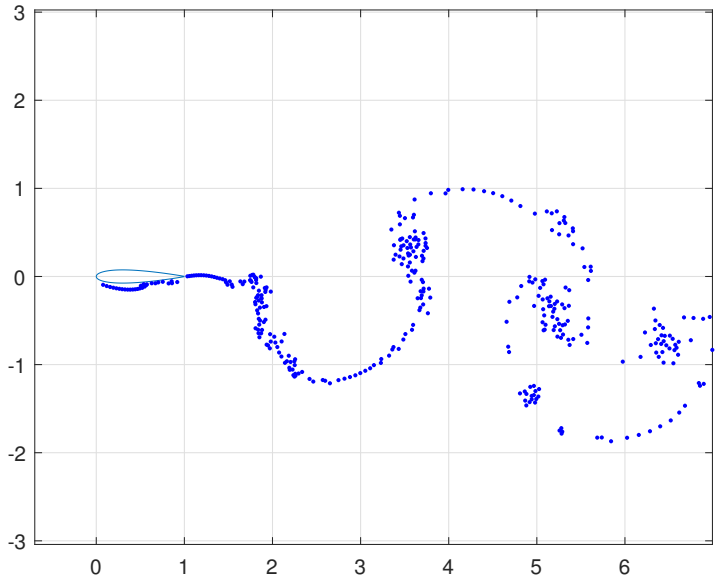

Fig. 7 Snapshot of vortices behind a heaving NACA0015 aerofoil at $Re = 1100$ and $k = 1.0$, and maximum amplitude of 0.6 u_∞. Axis in number of chords.

2. Heaving NACA0015 aerofoil

Here we illustrate the relation between v_{LE} and A_0 during leading-edge separation using a heaving NACA0015 aerofoil. At $Re = 1100$, the aerofoil experience stall by leading-edge separation and the the critical LESP value A_0 at this Reynolds number is quoted as 0.2, according to previous matching with high-order simulations[19]. Here the aerofoil undergoes heave motion at a reduced frequency of $k = 1.0$, with a maximum heave speed of 60% of the forward velocity. Again a discretisation of 121 point vortex elements is used for the aerofoil. Figure 7 illustrates the resulting wake vortices shed after the first cycle of the heaving motion.

Figure 8 plots the non-dimensional normal and tangential load exerted on the aerofoil, the value of the LESP A_0 through the heaving motion. Cases with and without leading-edge separation modelling are shown for comparison, and the effect of the leading-edge shedding on the aerodynamic loads is clearly seen. For the case with leading-edge separation, the normal component of the aerodynamic force remains close to the attached flow case due to the vortex lift generation mechanism from the nascent leading-edge vortex. However notable differences can be seen on the tangential component that indicates a change in the lift direction resulting a reduction of the propulsive effect, i.e. drag, in heaving motion due to the separation.

Figure 9 is a comparison of the computed value of A_0 against v_{LE}. It can be seen here that even for a thick aerofoil, the two measures exhibit a nearly linear relationship, and thus either value can be employed in the computation of LESP.

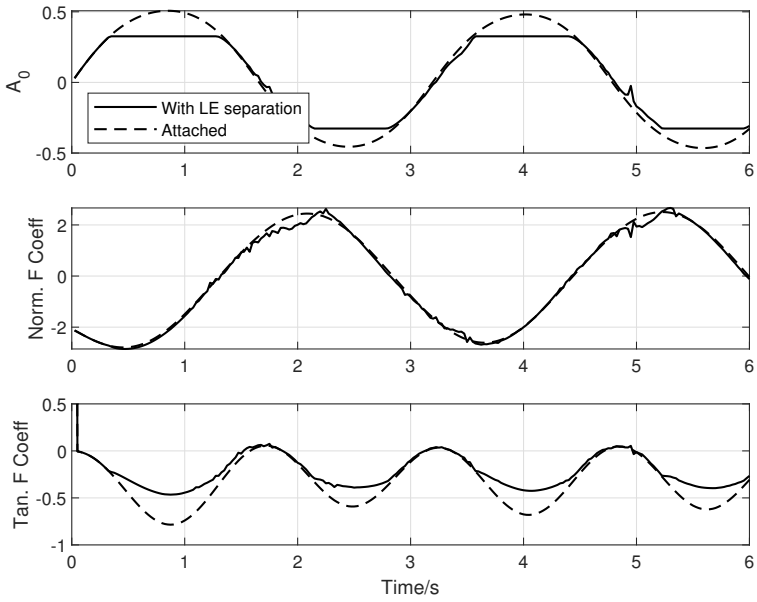

Fig. 8 The values of A_0, normal (vertical) and tangential (horizontal) force coefficients for the heaving aerofoil.

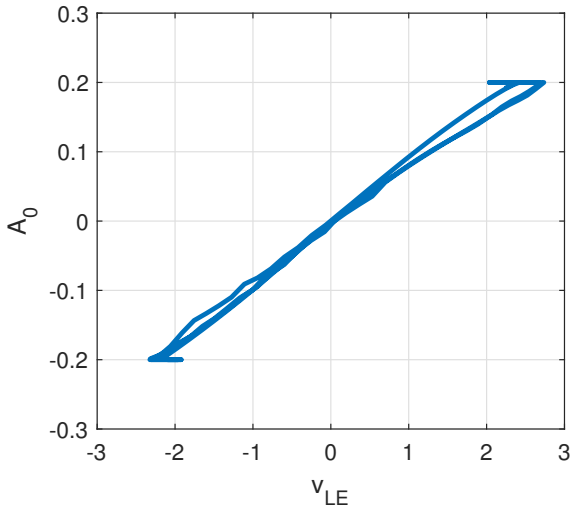

Fig. 9 Comparison of two measures of the leading-edge suction, A_0 against v_{LE}.

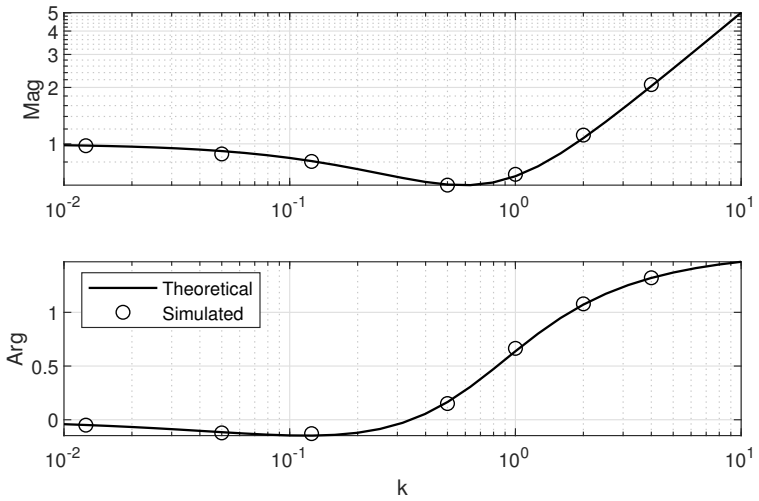

Fig. 10 Comparison of magnitude and phase of the non-dimensionalised lift response of thin aerofoil in sinusoidal heave at different values of the reduced frequencies k.

B. Flow around Slender Rectangular Wing

Next we use a high aspect ratio rectangular wing to verify both the attached and separated aerodynamics solutions against known results. The wing used in this test case has chord $c = 1$ m and area $A = 20$ m^2, and having the NACA0004 aerofoil. The wing is divided into a total of 120 panels chordwise around the aerofoil with cosine spacing, and 10 panels spanwise. One additional row of panels is used to close the wing tips on both upper and lower sides. The simulations use a non-dimensional timestep of $0.02/k$ for different values of the reduced frequency.

The fine chordwise discretisation in this example is due to the high reduced frequency ($k = 4$) attained in the linear simulation. As will be shown in the verification against both attached and separated flow cases, this discretisation leads to converged results.

1. Attached Flow under Heave

In this simulation, the wing is subject to small-amplitude sinusoidal heaving motion. The resulting aerodynamic forces will be compared against 2D theoretical solution from Theodorsen's function.

For a (high aspect ratio) wing of chord c and area A subject to uniform freestream velocity $\mathbf{v}_\infty$ (i.e. with a flow speed of $||\mathbf{v}_\infty||$ in the chordwise direction), and undergoing heaving motion of the form $h = h_0 e^{i\omega t}$, 2D thin aerofoil theory gives the form of the resultant lift on the wing as

$$L = -\pi\rho A||\mathbf{v}_\infty||(C(k) + ik/2)\dot{h} \tag{21}$$

where $C(k)$ is the Theodorsen's lift deficiency function and the reduced frequency k is defined as $\omega = 2k||\mathbf{v}_\infty||/c$

Figure 10 shows the magnitude and phase of the resulting non-dimensional lift response for the sinusoidal heaving motion describe here, compared with the theoretical value of $C(k) + ik/2$, where the latter term arises from the added mass. This test case demonstrated the validity of the attached flow solver.

2. Flow with Leading-Edge Separation

In the second part of the test case, we demonstrate the separated flow solution on the rigid version of the wing. Here the wing suddenly experiences an impulsively started flow with 45 degrees angle of attack (the setup can be understood to be the flow that is impulsively started). This test case stipulates that the flow separates completely from the leading edge, making the value of LESPc (critical LESP) zero and reducing the leading edge to a Kutta condition.

Figure 11 shows the nondimentional normal force coefficient experienced at the central section of the wing, with 2D inviscid CFD (Euler) results by Li[25] as comparison. The 45 degree starting flow case is very well validated in the literature as a test case for both vortex and CFD methods. A good overall agreement is seen, but small oscillations are also present in some parts of the response, due to a combination of low-order discretisation of the solid body as vortex rings, and a lack of a finite vortex core in the current formulation. When singularity elements are advected close to lifting surfaces, the rapidly changing induced velocities will lead to such oscillations. Cored vortices are not currently used in this work as the STFMM fast multipole acceleration package does not support a finite vortex core.

Note here that flow in a truly inviscid fluid does not separate at all. However, due to finite discretisation in numerical simulations, a small amount of numerical viscosity is always present in the inviscid CFD result used for comparison, leading to full separation at the leading edge but without forming a viscous boundary layer of finite thickness.

Figure 12 is a convergence test for separated flow using the 45 degree case, over the same non-dimensional time period. The figure shows relative error against the number of chordwise panel discretisation and timestep, using a fine discretisation (non-dimensional timestep of 0.005, 240 panels) as baseline value. It can be seen that the discretisation error is not sensitive to chordwise panel count, and that reducing timestep correlates with a lower error up to a value of 0.25, at which point the above-mentioned fluctuations account for the remainder of the error. Here we can conclude that for the dynamic response of leading-edge separation on relatively thin aerofoils, a non-dimensional timestep of below 0.1 and a chordwise discretisation of more than 60 panels (total around the aerofoil) can be considered sufficiently converged under the current numerical scheme. This discretisation will be used in the subsequent simulations.

Finally, figure 13 shows the chordwise pressure coefficient distribution at various times. The steady ($\rho v^2/2$) and unsteady ($\rho d\Phi/dt$) contributions are also shown. It should be noted that in vortex-based formulations, the unsteady pressure term is computed from the time derivative velocity potential, which appears as an integral of the surface tangential velocities, as shown in (10). Thus, the addition of any constant term to the velocity potential will introduce a change in the unsteady component of the surface pressure in the form of a spurious hydrostatic pressure. However, this does not affect the load on closed bodies and can be safely ignored unless the exact values of surface pressure is sought,

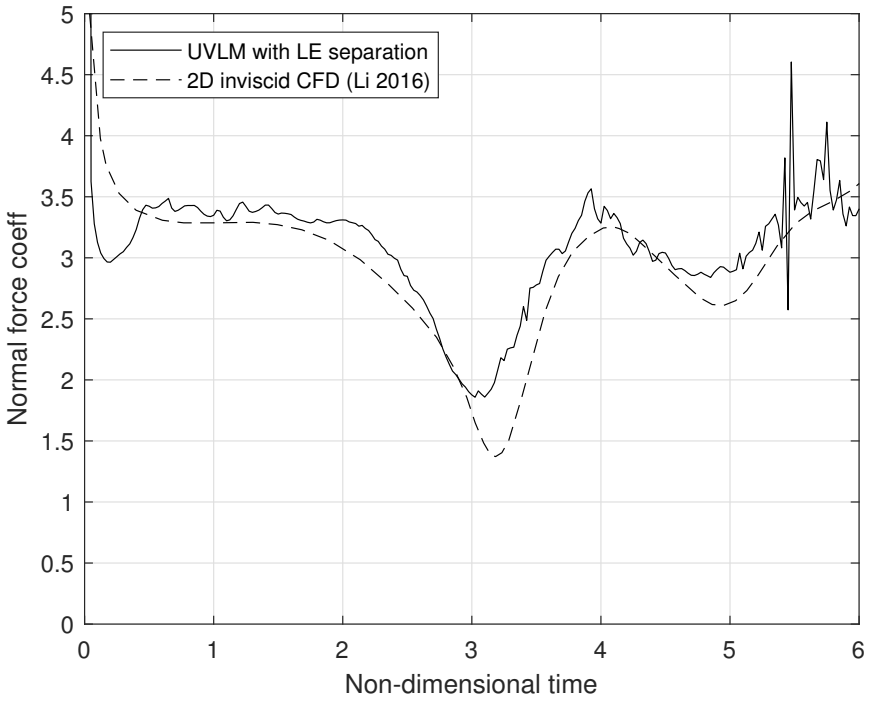

Fig. 11 Normal force coefficient for the suddenly started wing in 45° flow, compared with inviscid CFD result[25].

in which case a line integral to a point on the body from a far enough location upstream will be required to establish a relation against the reference pressure value. The test cases verify the validity of the 3D separated flow implementation as well as numerical convergence of the discretisation used.

C. Aeroelastic Response of Cantilever Wing

In this section, the aeroelastic solution will now be demonstrated on the Patil wing. The Patil wing is a high aspect ratio cantilever wing that is part of an aeroelastic test case, first proposed by Patil[26] and later used by Murua[27], that describes a 32-m wingspan HALE UAV flying at at an altitude of 20km. In this work we will use its parameters in a cantilever wing setup only. The parameters for the wing are presented in Table 2. It should be noted that a flat-plate aerofoil was assumed in the original work, but here a NACA0012 aerofoil is used as the current implementation requires a finite aerofoil thickness. As the case is static attached flow, 40 chordwise panels are used.

A 3D attached, quasi-static aeroelastic simulation is conducted. The test case[27] specifies the wing to be flying at 25 m/s in air with density of 0.0889 kg/m, and with angles of attack of 2° and 4°. Due to the change of aerofoil from a flat plate to NACA0012, the air density is scaled in this test case in order to compensate for the change in lift coefficient

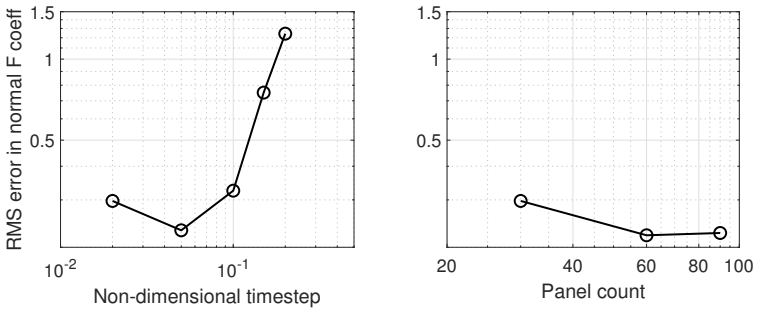

Fig. 12 Discretisation error in normal force coefficient, for different timesteps (left, with 240 panels) and panel counts (right, with non-dimensional timestep of 0.005), computed for the 45-degree starting flat plate.

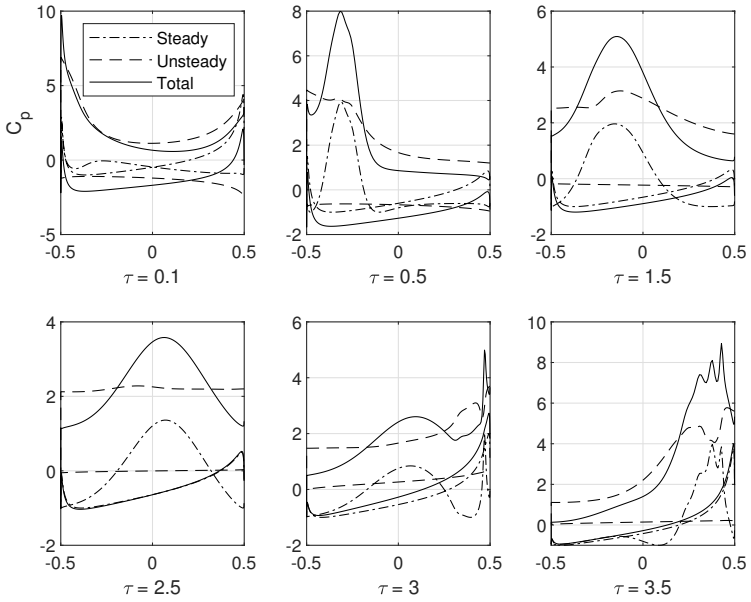

Fig. 13 Pressure coefficients for the suddenly started rigid wing in 45° flow at various times, plotted against chordwise position on aerofoil section.

Semispan	16 m
Chord	1 m
Elastic Axis	50% chord
C.G.	50% chord
Mass	0.75 kg/m
Sectional inertia	0.1 kg·m
Out-of-plane bending stiffness EI_2	1×10^4 Nm^2
In-plane bending stiffness EI_3	2×10^5 Nm^2
Torsional stiffness GJ	5×10^6 Nm^2

Table 2 Structural parameters of the Patil wing

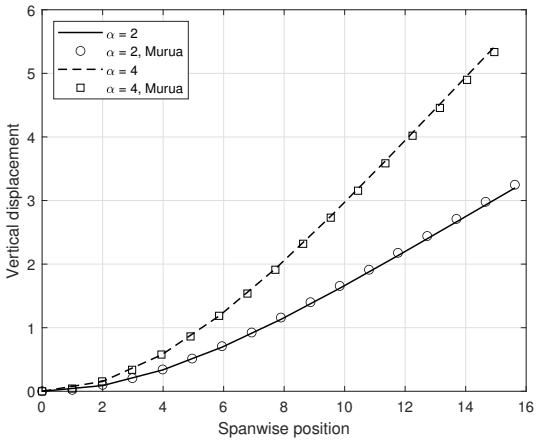

Fig. 14 Static deflections of the Murua wing, at 2 and 4 degrees of angle of attack. Reference data is from Werter[28].

(inviscid $C_{L\alpha} = 6.88$ for NACA0012 compared to 6.28 for a flat plate).

Figure 14 is a plot of the resulting bending deformation for the cases described above. These have been simulated as a damped steady-state dynamic response. Due to the location of the elastic axis, the Murua wing is extremely sensitive to torsional deformation and the 3D tip effect. It is well known that 2D strip theory fails to capture the correct deformation in this verification test case despite the high aspect ratio of this particular wing. It can be seen from the simulation that the deformations have been captured very well when compared to previous results by Werter[28] with thin aerofoil UVLM, verifying the validity of the 3D attached aeroelastic solution.

D. Flutter and Limit-Cycle Oscillation on Goland Wing

The Goland wing [29] is a low aspect ratio rectangular cantilever wing whose flutter response serves as a standard test case for linear aeroelastic simulation. This example will be used here to both verify the code and demonstrate the simulation of limit-cycle oscillation.

The structural and aerodynamic parameters of the Goland wing are listed in Table 3. Here, λ is the distance between the sectional centre of mass axis and the elastic axis (forward of the c.m.), whereas a is the distance between the elastic axis and the aerodynamic centre (forward of the e.a.).

The Goland wing is defined as a flat plate aerofoil with the a.c. located at 25% chord. As the current model requires non-zero thickness, a NACA0006 aerofoil is used to minimise the difference in $C_{L\alpha}$ with the flat plate. The fluid is assumed to be incompressible as in referenced works on this test case. In this test case, a separate simulation based on geometrically-exact beam solver and a 2D panel method employing the critical LESP separation model is also used as a comparison. For both models, the lifting surface is discretised into 60 chordwise panels and 8 spanwise segments. A

Span	6.096m
Chord	1.8488m
Air density	1.02 kg/m^3
Bending stiffness EI_3	9.77×10^6 Nm^2
Torsional stiffness GJ	0.99×10^6 Nm^2
Mass density ρA	35.71 kg/m
Sectional inertia ρI_1	8.64 kgm
Distance of e.a. to a.c., a	0.1463 m
Distance of c.m. to e.a., λ	0.18288 m
Aerofoil	Ideal flat plate

Table 3 Properties of the Goland wing.

Model	V_f, m/s	ω_f, rad/s
Present 2D, Intrinsic + vortex panel methods	150	70.0
Present 3D, Intrinsic + UVLM	165	69.7
Palacios et al.[31], Intrinsic + Inflow	141	69.8
Murua et al.[30], Displacement + UVLM	165	69.7

Table 4 Flutter velocities and frequencies of the Goland wing.

timestep of 0.001s is used, corresponding to a non-dimensional timestep of 0.08 at 150 m/s. The reduced frequency for flutter is around 0.4.

1. Flutter

First, we present linear flutter result for 2D and 3D simulations which serves as a model verification against existing results. The simulated flutter velocity and resulting flutter frequencies are shown in Table 4.

A number of effects can be seen in the comparison. The 2D strip theory formulations used in the referenced works did not include the effect of added mass, and therefore resulted in a lower flutter velocity than the 2D vortex panel method used here. Also, due to the absence of tip loss, the flutter velocity in all 2D simulation is significantly lower than that in the 3D simulation, as a result of much higher aerodynamic loads at the wingtip. The 3D flutter velocity recovers the results from previous simulations using UVLM[30].

2. Limit-Cycle Oscillation

If the flutter on the Goland wing is allowed to grow, a limit-cycle oscillation (LCO) will eventually establish itself. A freestream velocity of 180m/s, beyond the flutter velocity of both 2D and 3D models, is used here to illustrate the LCO. As the Goland wing did not originally specify an aerofoil or a Reynolds number, a critical LESP (A_0) value of 0.15 is selected to demonstrate the effect of leading-edge separation.

In figure 15, the aerodynamic loads experienced at mid-chord are plotted for a location at half span along the

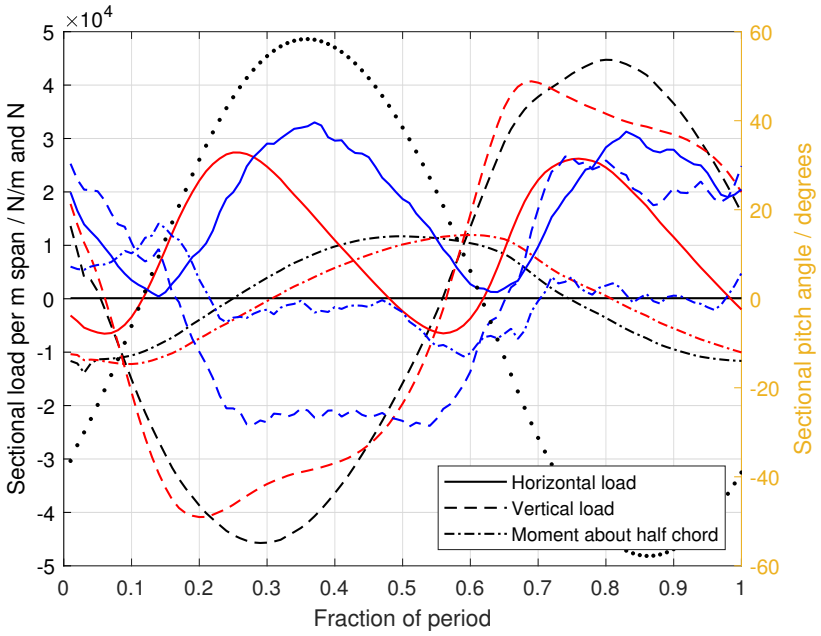

Fig. 15 2D strip-theory aerodynamic load in inertial frame at half span about mid-chord. Black: linear small disturbance. Red: fully attached flow. Blue: with separation. Also shown is the rotation of the wing section during a period (dotted black line).

the beam, using data from the 2D strip theory simulation. The horizontal direction is defined as the direction of the freestream flow. Here 2D data is used so that a fair comparison can be made using 2D fully attached flow, as well as linear unsteady aerofoil theory (i.e. Theodorsen's response), for the same kinematics in the LCO. Even when only the attached flow is simulated, the shift in the direction of lift away from the aerofoil normal direction at large angles of attack will introduce such an LCO, as can be seen between the difference of attached and linear results in horizontal and vertical loads. In general this LCO is much higher in amplitude than what can be observed experimentally or if a separated flow model is used, as nonlinear aerodynamic effects will set in long before this theoretical LCO (attached aerodynamic force) is reached. In contrast, if leading-edge separation is modelled, its effect on the formation of LCO on an aerofoil section can be briefly understood as follows. First, flow separation results in a much lower lift in general after the initial separation transient than the attached flow value, reducing the energy extracted from the flow in each oscillation cycle. A second effect is a shift in the (average) centre of lift towards the downstream direction when separation takes place, as can be seen in the dramatic reduction in pitching moment. This serves to pitch the local aerofoil back into the flow direction, also reducing the amplitude in the flutter mode. Whenever large instantaneous angles of attack is present, both these effects counters the otherwise exponential growth of the unstable linear flutter mode. This results in an LCO that reflects the onset of flow separation on each aerofoil section. An additional effect can also be observed, that is, a very significant lag in the lift response (around 15% of the cycle period) arising from the

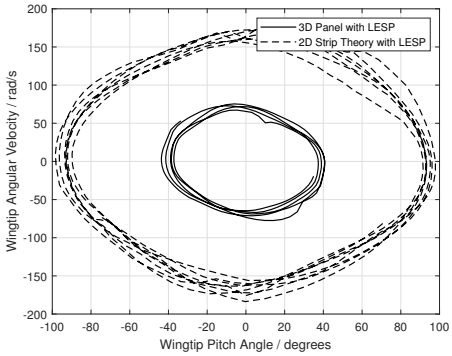

Fig. 16 Comparison of the phase portrait for the limit-cycle oscillation of the Goland wing at 180 m/s with a critical LESP value of 0.15, computed using strip theory with LESP (2D model) and vortex panels with LESP (3D model). The wingtip pitch angle and pitch rate are plotted here.

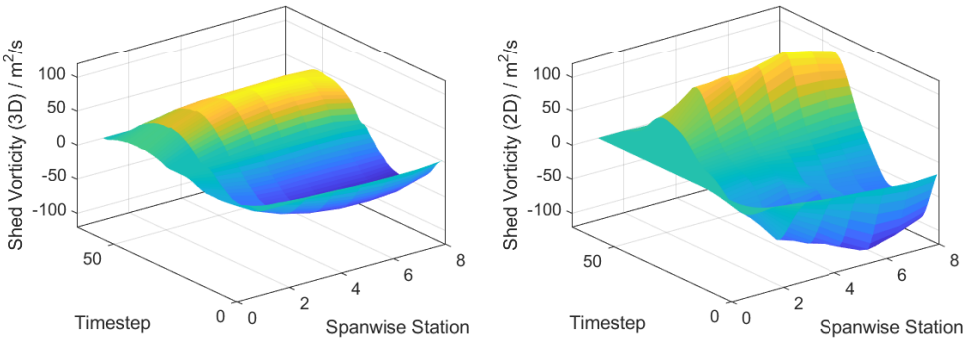

Fig. 17 Strength of the leading-edge vortex shed at each timestep during a limit cycle.

formation and shedding of leading-edge vortices along the aerofoil surface.

As can be expected from the large difference between 2D and 3D flutter velocities, the results demonstrate that the simulated LCO behaviour is also strongly affected by the 3D (spanwise) interactions. Figure 16 is a comparison of the resulting limit-cycle oscillation by plotting the wingtip pitch angle. Although the results are simulated under identical leading-edge separation criteria, one can immediately see that the 2D limit cycle exhibit a significantly larger oscillation, up to 95 degrees as opposed to 40 degrees for the 3D simulation. The ability to capture the effect of the spanwise interaction on the resulting behaviour is one of the key features of the proposed method. Despite the presence of such interactions and visible rollup of the wingtip wake in the spanwise direction, only a small spanwise flow velocity of less than 20m/s (for a freestream velocity of 180m/s) is observed on the leading edge itself, indicating that the 3D interactions in this test case still consists mostly of wake-induced velocity in the normal or chordwise direction, in a way similar to that in an attached UVLM simulation.

Figure 17 shows the strength of the newly shed leading-edge vorticity at each timestep. One can see that leading-edge separation is present to some extent over most part of the limit cycle, indicated by a non-zero shed vorticity, which

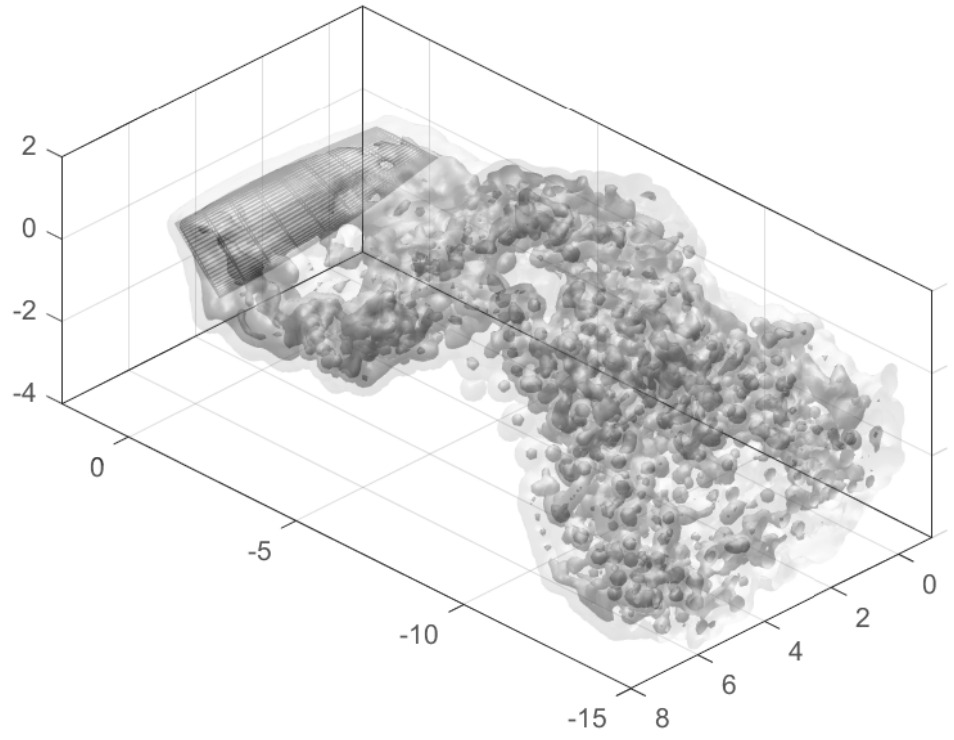

Fig. 18 Flow field visualisation of the limit-cycle oscillation on the Goland wing in 3D. Vorticity contours are of 100, 10000 and 40000 s^{-1} from light to dark respectively.

agrees with the observation that the oscillation in sectional angle-of-attack is very high. Attached flow condition can be observed for a very short period each time the shed vorticity crosses over. Figure 18 shows the vorticity distribution isosurface at a typical instance in the limit cycle. It is created by converting the wake vortex ring elements into a volumetric vorticity distribution. One should note that the figure is simply another way to render the wake in a panel method. This is so that the actual vorticity distribution is shown rather than simply showing the structure of the vortex elements themselves (as is normally done in panel formulations). The figure illustrates a number of flow features in the limit cycle. One can see a sheet of newly formed leading-edge vortex envelopes most of the upper surface of the wing but has yet to detach into the wake. Also visible is the wingtip vortex rolling up behind the upper wing surface at the tip and interacting strongly with the wake further downstream. The low vorticity regions in the wake are shed at instances where the local aerofoil is at small angles of attack.

E. Deployment of Folding Wing

In this final example, we consider the in-flight deployment of a low-aspect ratio folding wing system, described first by Otsuka et al[32]. This case is selected to demonstrate the ability of the solver to simulate cases when there is

Span per section	150 mm
Width	50 mm
Thickness	2 mm
Density	1420 kg/m^3
Young's modulus E	2.83 GPa
Torsional stiffness GJ	0.18 Nm^2
Hinge stiffness	0.026 Nm/rad
Hinge torque at full extension	0.043 Nm
Initial fold angle	170°

Table 5 Properties of the folding wing.

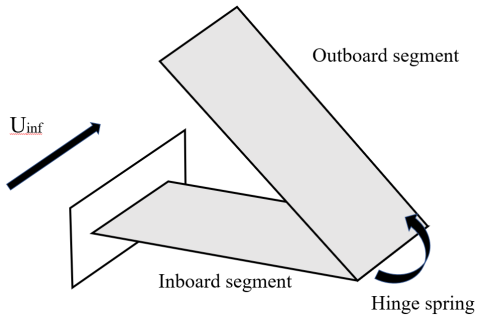

Fig. 19 Illustration of the folding wing system.

proximity between lifting surfaces.

The folding wing, shown in figure 19, consists of a cantilever wing section with a spring-loaded hinge in the middle. The outboard section can be deployed from a initially folded state, rotating under the spring torque and eventually forming a straight cantilever wing. Once straight, a lock then holds the outboard wing in place. The structural properties of the setup are shown in Table 5. Here 'full extension' refers to the state in which the outboard section is aligned with the inboard section and which the tip is at maximum distance from the base of the cantilever. Note the non-zero hinge holding torque at full extension.

In this simulation we selected the case where the freestream velocity is 5m/s, under which condition the speed of the deploying section meant that significant separation will be taking place. A critical LESP value of 0.2 is used, corresponding to a thin aerofoil approaching that of a flat plate.

Figure 20 and 21 plots the value of LESP and the pressure difference between upper and lower surfaces on the outer section of the wing respectively. The tip reaches an angle of attack of more than 50 degrees. It can be seen clearly from the LESP value that different sections of the outboard wing separate and reattach at different points in time, with associated changes in the pressure distribution. Capturing the 3D effects associated with intermittent separation of different sections of the wing is a key point in the current method.

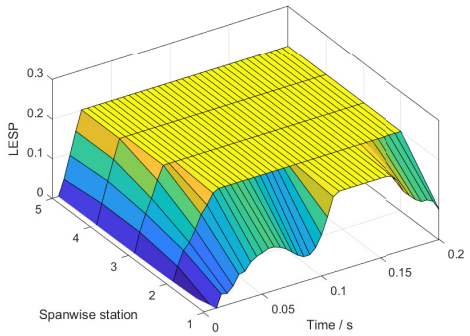

Fig. 20 Variation in the value of LESP with time on the outer section.

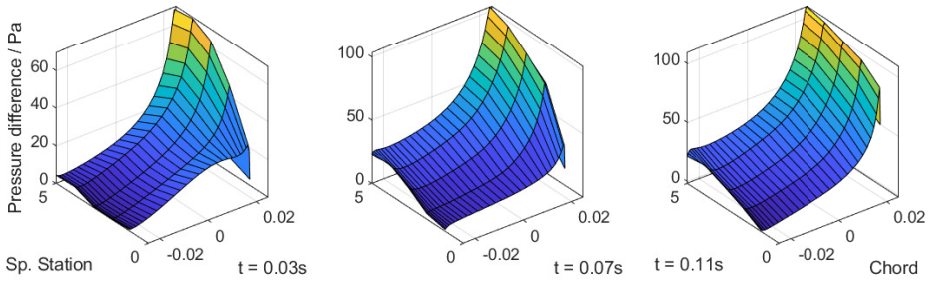

Fig. 21 Distribution of pressure difference between upper and lower surfaces at selected instants in time, plotted against chordwise and spanwise directions.

Figure 22 is an illustration of the flow field using the vorticity distribution, at various instants in time. The rollup of the wingtip separation sheet can be seen clearly. In Figure 23, the displacement of the *inboard* section at 50% chord and at a location of 10cm from the base, for simulations with and without the inclusion of leading-edge separation is shown. It can be seen that the reduction in lift due to separation reduces the deployment time compared to a fully attached flow, however due to the low freestream velocity and the vortex-generated lift after initial separation, the effect is not very significant. Also shown is a set of experimental data of the setup[32]. Note that the experimental setup locks the hinge once full extension is reached, this detail is not present in the current model and results in the difference in the response after full deployment at 0.11s. Also, the outboard section is initially held at the tip in the experimental setup, whereas the current model holds the hinge angle instead, giving rise to a different initial transient response.

V. Conclusions

In this work, we have proposed a coupled dynamic aeroelastic solver incorporating a modified unsteady panel method suitable for computing intermittently separating 3D flows around slender aero-structures. This is achieved by modelling leading-edge separation using the critical LESP parameter. Numerical verifications are made against a number of 2D

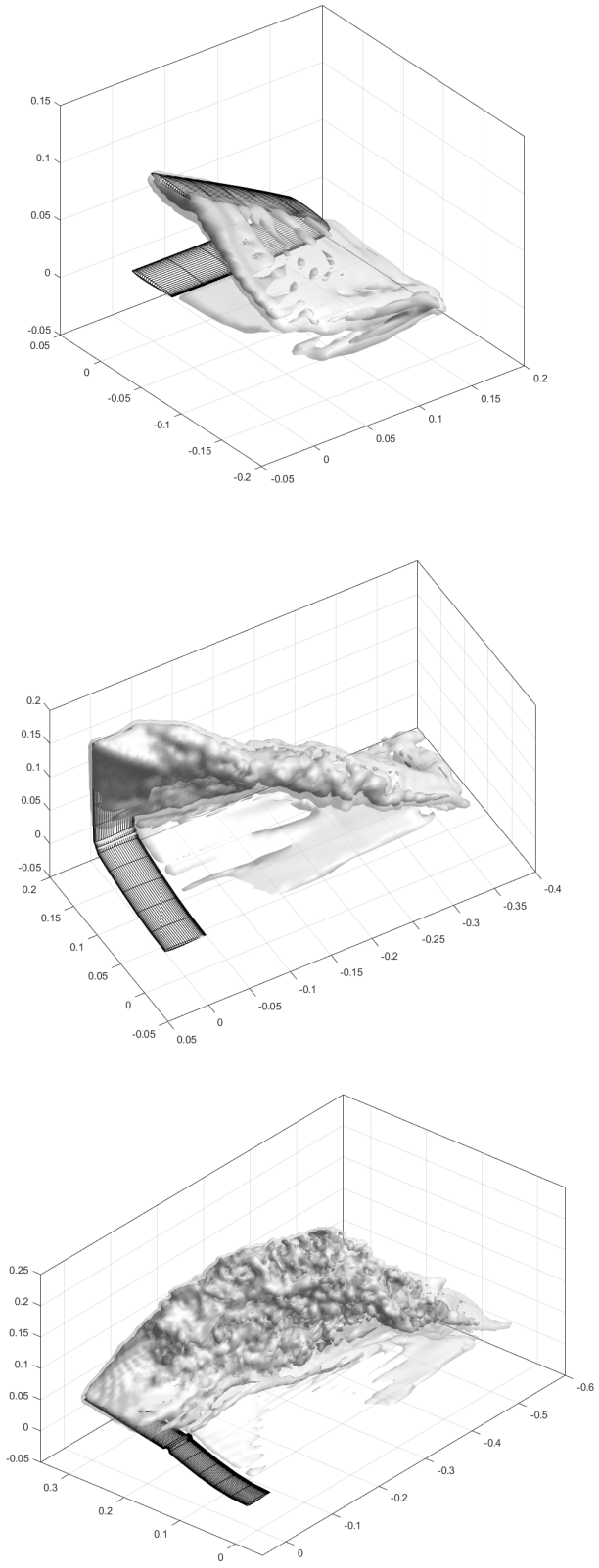

Fig. 22 Vorticity contours at selected instants in time. From top: 0.03 s, 0.07 s and 0.11 s since initial release. Axis unit in m. For clarity the figures is presented from different viewing angles.

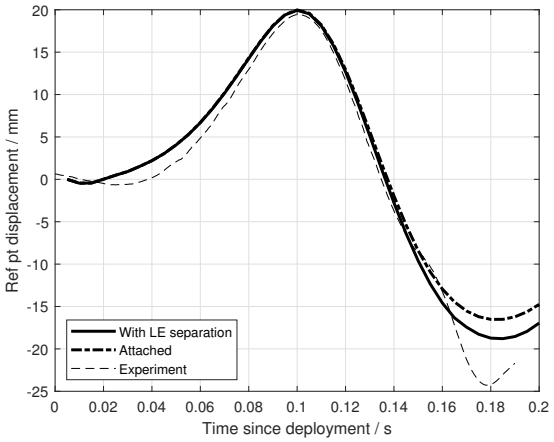

Fig. 23 Displacement of the inboard segment at 10 cm from the root, compared to attached flow computation and experimental data by Otsuka[32]. Positive displacement is upwards (for an upwards deploying outer section).

and 3D test cases for both attached and separated flows. We further show that the method is capable of simulating 3D dynamic limit-cycle responses on complex geometries. The results highlighted the importance of including 3D flow effects in simulating dynamic flow separation in the aeroelastic responses of slender lifting surfaces. All simulations are completed on a 16-core workstation in under 12 hours, demonstrating the low computational requirement for the method.

The method could greatly reduce the time to simulate limit-cycle oscillation on high-aspect ratio wings, as well as opening up new ways to study the aeroelasticity of moderate aspect-ratio flapping wings. It should be noted here that the LESP model is but one of many models on the prediction of dynamic stall onset, which was chosen based on its simplicity and compatibility with UVLM. Ultimately one should expect a dynamic boundary layer model to be used, in order to provide more accurate predictions of separation location and onset without the need for additional information such as the critical LESP value.

Acknowledgements

This project is supported by the U.K. Leverhulme Early Career Fellowship, Grant ECF-2018-727. The second author is funded by the UK Engineering and Physical Sciences Research Council, Grant EP/S000747/1. Their support is gratefully acknowledged.

References

[1] Maraniello, S. and Palacios, R., "State-space realizations and internal balancing in potential-flow aerodynamics with arbitrary kinematics," *AIAA Journal*, Vol. 57, No. 6, 2019, pp. 2308–2321, doi:10.2514/1.J058153.

[2] Ritter, M., Teixeira, P., and Cesnik, C. E., "Comparison of nonlinear aeroelastic methods for maneuver simulation of very

flexible aircraft," *2018 AIAA/ASCE/AHS/ASC Structures, Structural Dynamics, and Materials Conference*, 2018, p. 1953, doi:10.2514/6.2018-1953.

[3] Ramos-García, N., Sørensen, J. N., and Shen, W. Z., "Three-dimensional viscous-inviscid coupling method for wind turbine computations," *Wind Energy*, Vol. 19, No. 1, 2016, pp. 67–93, doi:10.1002/we.1821.

[4] Ng, B. F., Palacios, R., Kerrigan, E. C., Graham, J. M. R., and Hesse, H., "Aerodynamic load control in horizontal axis wind turbines with combined aeroelastic tailoring and trailing-edge flaps," *Wind Energy*, Vol. 19, No. 2, 2016, pp. 243–263, doi:10.1002/we.1830.

[5] Fleischmann, D., Weber, S., and Lone, M. M., "Fast computational aeroelastic analysis of helicopter rotor blades," *2018 AIAA Aerospace Sciences Meeting*, 2018, p. 1044, doi:10.2514/6.2018-1044.

[6] Wang, Z., Chen, P. C., Liu, D. D., and Mook, D. T., "Nonlinear-aerodynamics/nonlinear-structure interaction methodology for a high-altitude long-endurance wing," *Journal of Aircraft*, Vol. 47, No. 2, 2010, pp. 556–566, doi:10.2514/1.45694.

[7] Parenteau, M., Plante, F., Laurendeau, E., and Costes, M., "Unsteady Coupling Algorithm for Lifting-Line Methods," *55th AIAA Aerospace Sciences Meeting*, 2017, p. 0951, doi:10.2514/6.2017-0951.

[8] Gamble, L. L., Pankonien, A. M., and Inman, D. J., "Stall recovery of a morphing wing via extended nonlinear lifting-line theory," *AIAA Journal*, 2017, pp. 2956–2963, doi:10.2514/1.J055042.

[9] Leishman, J. G. and Beddoes, T., "A Semi-Empirical model for dynamic stall," *Journal of the American Helicopter society*, Vol. 34, No. 3, 1989, pp. 3–17, doi:10.4050/JAHS.34.3.3.

[10] Hansen, M. H., Gaunaa, M., and Madsen, H. A., "A Beddoes-Leishman type dynamic stall model in state-space and indicial formulations," *Geology*, 2004.

[11] Tran, C. and Petot, D., "Semi-empirical model for the dynamic stall of airfoils in view of the application to the calculation of responses of a helicopter blade in forward flight," *ONERA*, 1980.

[12] Tang, D. and Dowell, E. H., "Comments on the ONERA stall aerodynamic model and its impact on aeroelastic stability," *Journal of fluids and structures*, Vol. 10, No. 4, 1996, pp. 353–366, doi:10.1006/jfls.1996.0023.

[13] Drela, M. and Giles, M. B., "Viscous-inviscid analysis of transonic and low Reynolds number airfoils," *AIAA journal*, Vol. 25, No. 10, 1987, pp. 1347–1355, doi:10.2514/3.9789.

[14] Drela, M., "XFOIL: An analysis and design system for low Reynolds number airfoils," *Low Reynolds number aerodynamics*, Springer, 1989, pp. 1–12, doi:10.1007/978-3-642-84010-4_1.

[15] Veldman, A., "Quasi-simultaneous viscous-inviscid interaction for transonic airfoil flow," *4th AIAA Theoretical Fluid Mechanics Meeting*, 2005, p. 4801, doi:10.2514/6.2005-4801.

[16] Katz, J., "A discrete vortex method for the non-steady separated flow over an airfoil," *Journal of Fluid Mechanics*, Vol. 102, 1981, pp. 315–328, doi:10.1017/S0022112081002668.

[17] Nelson, B. and Kouh, J.-S., "The numerical analysis of wind turbine airfoils at high angles of attack," *International Journal of Energy and Environmental Engineering*, Vol. 7, No. 1, 2016, pp. 1–12, doi:10.1007/s40095-015-0197-6.

[18] Prasad, C. S. and Dimitriadis, G., "Application of a 3D unsteady surface panel method with flow separation model to horizontal axis wind turbines," *Journal of Wind Engineering and Industrial Aerodynamics*, Vol. 166, 2017, pp. 74–89, doi:10.1016/j.jweia.2017.04.005.

[19] Ramesh, K., Gopalarathnam, A., Granlund, K., Ol, M. V., and Edwards, J. R., "Discrete-vortex method with novel shedding criterion for unsteady aerofoil flows with intermittent leading-edge vortex shedding," *Journal of Fluid Mechanics*, Vol. 751, 2014, pp. 500–538, doi:10.1017/jfm.2014.297.

[20] Katz, J. and Plotkin, A., *Low-Speed Aerodynamics*, Cambridge University Press, 2001.

[21] Morgenthal, G. and Walther, J., "An immersed interface method for the Vortex-In-Cell algorithm," *Computers and Structures*, Vol. 85, 2007, pp. 712–726, doi:10.1016/j.compstruc.2007.01.020.

[22] Tornberg, A.-K. and Greengard, L., "A fast multipole method for the three-dimensional Stokes equations," *Journal of Computational Physics*, Vol. 227, No. 3, 2008, pp. 1613–1619, doi:10.1016/j.jcp.2007.06.029.

[23] Wang, Y., Wynn, A., and Palacios, R., "Nonlinear Modal Aeroservoelastic Analysis Framework for Flexible Aircraft," *AIAA Journal*, 2016, pp. 1–16, doi:https://doi.org/10.2514/1.J054537.

[24] Eldredge, J., Wang, C., and Ol, M., "A computational study of a canonical pitch-up, pitch-down wing maneuver," *39th AIAA fluid dynamics conference*, 2009-3687, doi:10.2514/6.2009-3687.

[25] Li, J. and Wu, Z., "A vortex force study for a flat plate at high angle of attack," *Journal of Fluid Mechanics*, Vol. 801, 2016, pp. 222–249, doi:10.1017/jfm.2016.349.

[26] Smith, M. J., Patil, M. J., and Hodges, D. H., "CFD-based analysis of nonlinear aeroelastic behavior of high-aspect ratio wings," *19th AIAA Applied Aerodynamics Conference*, Vol. 1582, 2001, p. 2001, doi:10.2514/6.2001-1582.

[27] Murua, J., Palacios, R., and Graham, J. M. R., "Assessment of Wake-Tail Interference Effects on the Dynamics of Flexible Aircraft," *AIAA Journal*, Vol. 50, No. 7, 2012, pp. 1575–1585, doi:10.2514/1.J051543.

[28] Werter, N. and De Breuker, R., "A novel dynamic aeroelastic framework for aeroelastic tailoring and structural optimisation," *Composite Structures*, Vol. 158, 2016, pp. 369–386, doi:10.1016/j.compstruct.2016.09.044.

[29] Goland, M., "The Flutter of a Cantilever Wing," *Journal of Applied Mechanics*, Vol. 12, No. 4, 1945, pp. 197–208, doi:10.1115/1.4009489.

[30] Murua, J., Palacios, R., and Graham, J. M. R., "Modeling of Nonlinear Flexible Aircraft Dynamics Including Free-Wake Effects," *52nd AIAA/ASME/ASCE/AHS/ASC Structures, Structural Dynamics, and Materials Conference*, April 2011, doi: 10.2514/6.2010-8226.

[31] Palacios, R. and Epureanu, B. I., "An Intrinsic Description of the Nonlinear Aeroelasticity of Very Flexible Wings," *52th AIAA/ASME/ASCE/AHS/ASC Structures, Structural Dynamics, and Materials Conference*, April 2011, doi:10.2514/6.2011-1917.

[32] Otsuka, K., Wang, Y., Fujita, K., Nagai, H., and Makihara, K., "Multifidelity Modeling of Deployable Wings: Multibody Dynamic Simulation and Wind Tunnel Experiment," *AIAA Journal*, Vol. 57, No. 10, 2019, pp. 4300–4311, doi:10.2514/1.J058676.